Research Square

Preprints are preliminary reports that have not undergone peer review.
They should not be considered conclusive, used to inform clinical practice,
or referenced by the media as validated information.

# Gate-Engineered High-Performance Triple Material Gate AlGaN/GaN HEMT based Biosensor for pH Detection

**E. Raghuveera**

e.raghuveer@hotmail.com

National Institute of Technology Silchar

**Padmakshya Kar**

National Institute of Technology Silchar

**Nitish Kumar**

National Institute of Technology Silchar

**Trupti Ranjan Lenka**

National Institute of Technology Silchar

**Hieu Pham Trung Nguyen**

Texas Tech University

**Research Article**

**Keywords:** Gate-engineered HEMT, Biosensor sensitivity, AlGaN/GaN, 2DEG modulation, pH sensor

**Posted Date:** April 29th, 2026

**DOI:** https://doi.org/10.21203/rs.3.rs-9444401/v1

**License:** This work is licensed under a Creative Commons Attribution 4.0 International License.
Read Full License

**Additional Declarations:** No competing interests reported.

**Version of Record:** A version of this preprint was published at Microsystem Technologies on July 21st, 2026. See the published version at https://doi.org/10.1007/s00542-026-06099-w.

# Gate-Engineered High-Performance Triple Material Gate AlGaN/GaN HEMT based Biosensor for pH Detection

E. Raghuveera[1], Padmakshya Kar[1], Nitish Kumar[1], Trupti Ranjan Lenka[1], and Hieu Pham Trung Nguyen[2]

[1]Department of Electronics & Communication Engineering, National Institute of Technology Silchar, Assam, India,
Email: trlenka@ieee.org
[2]Department of Electrical and Computer Engineering, Texas Tech University, Lubbock, Texas, 79409, USA
Email: hieu.p.nguyen@ttu.edu

Abstract—The gate-engineered AlGaN/GaN HEMT with an AlN cap layer is proposed in this article for detecting potential hydrogen (pH). In this work, we introduce three different gate structures: Single Material Gate (SMG), Double Material Gate (DMG), and Triple Material Gate (TMG) for pH detection. The drain current sensitivity analysis is carried out for all three structures. We demonstrate the sensing mechanism used for three structures, and the Silvaco ATLAS TCAD simulation tool is employed to extract the relevant parameters. There is a significant improvement in the drain current (Id) and transconductance ($g_m$) of the gate material-engineered structures over the conventional single-material gate structures due to the changes in the surface potential of the channel. The proposed gate-engineered HEMT is used to detect the pH values ranging from 2 to 9. A sensitivity analysis was conducted for all three structures. Three structures showed better current sensitivities SI (SMG) = 23.20mA/mm/pH, SI (DMG) = 21.52mA/mm/pH and SI (TMG) = 19.81mA/mm/pH. The three devices exhibit better linearity, with a coefficient of determination ($R^2$) of > 0.96. The voltage sensitivities were also determined as SV (SMG) = 44.2 mV/pH, SV (DMG) = 36.4 mV/pH, and SV (TMG) = 49.1 mV/pH at 10mA/mm, exhibiting good linearity, with a coefficient of determination ($R^2$) = 1, which confirms their pH detection capability, reliability, and robustness. These devices exhibit higher sensitivities in alkaline regions, comparable to those in acidic areas. The TMG structure with an AlN cap layer is a more suitable candidate for high-performance, high-linearity, and robust pH sensing applications.

Index terms—Gate-engineered HEMT, Biosensor sensitivity, AlGaN/GaN, 2DEG modulation, pH sensor

## I. INTRODUCTION

Due to the advancements in technology in various fields of science and engineering, the life of humans has become very simple and easy. These developments in technology have brought lots of changes to their lifestyles. On the other hand, these technological developments brought many societal problems like pollution, global warming, etc., due to which the average life span of the human being has been reduced. As per data reported by the World Health Organisation (WHO), in India, the life expectancy at birth was 67.3 years in 2021. The key reason for the above is the evolution of various diseases, cancers, and viruses, the primary cause of death in India due to the novel coronavirus COVID-19, officially named SARS-CoV-2, which stands for severe acute respiratory syndrome. In addition, deaths due to various cancers, heart diseases, Chronic obstructive pulmonary disease, Stroke, Diarrhoeal diseases, Lower respiratory infections, Diabetes mellitus, and tuberculosis have been very critical and dangerous. The early detection of these viruses is challenging and has led to numerous developments in biomedical engineering. The detection of these viruses/biomolecules is challenging, leading to the development of biosensors. The National Library of Medicine (NLM), a National Centre for Biotechnology Information, reported that the number of publications in the field of biosensors is 85174 in Web of Science as of 8th May 2019[1]. Biosensors were developed in specific fields (physics, chemistry and biology) in the early days; now, the field is a multidisciplinary area of research bridging the principles of sciences and the fundamental micro/nanotechnology, electronics and applicatory medicine. High electron mobility transistors (HEMTs) are predominantly used in most biosensors due to their superior performance characteristics[2], [3], [4]. This paper focuses on gate-engineered AlGaN/GaN HEMT biosensors; the gate structure of the HEMT is engineered to optimize the electrical behaviour of the device, and the same is used for detecting biomolecules. In literature, several gates engineered HEMT structures have been developed. The gate material engineered AlInN/GaN Double Gate MOSFET with Dual Material Gate (DMG) is proposed, and the same is compared with the Single Material Gate (SMG), and it is demonstrated that the performance of the DMG DM MOSFET improved over the SMG DG MOSFET.[5]. G. Purnachandra Rao et al. designed a novel gate-engineered HEMT on β-$Ga_2O_3$ substrate with three different gate structures. The effect of these gate structures on the electric field distribution, transfer, and I-V characteristics is presented, and a comparative analysis is performed on these gate structures [6]. The gate-engineered triple material gate AlGaN/GaN HEMT heterostructure analytical model was developed for channel potential and threshold voltage. The performance of the device is enhanced over the conventional HEMT structures.[7]. The impact of gate engineering on the gate material of enhancement mode $n^{++}$ GaN/InAlN/AlN/GaN HEMT proposed by Sarosij Adak *et al.*, the performance of the device is anlyzed for some key design parameters of the HEMT with Tripple Material Gate (TMG), Double Material Gate (DMG) and Single Material Gate (SMG) structures, the device dimensions are exact for all the mentioned gate structures and is observed that, the key device parameters are improved.[8]. The field-plated and recessed gate III nitride nano-HEMT on β-$Ga_2O_3$ substrate is developed. In this article, the channel length, gate length and suitable gate position is chosen for optimization and have shown better improvement in DC and RF characteristics towards high power and THz applications.[9]. The recessed gate HEMT structure developed using piezoelectric neutralization is analyzed for different recess depths of the gate, and it is shown that the HEMT proposed is efficient than the conventional HEMT.[10]. A low band gap InGaN layer near the heterointerface of the recessed gate AlGaN/GaN HMET is added to optimize the 2-dimensional electron gas (2DEG). There is a remarkable improvement in the density of the electrons at the heterointerface due to the addition of the InGaN layer.[11]. The field-plate and the recessed gate III-nitride nano HEMTs are designed, a β-$Ga_2O_3$ substrate is used to design the structure, the 2DEG density is characterized with and without an AlN spacer layer, it is observed that the large band offset, strong polarization field and increased barrier improve the 2DEG concentration in the presence of an AlN spacer layer.[12]. The paper is organized as follows: Section I gives the

introduction, Section II discusses the gate-engineered HEMT biosensor state of the art, Section III describes the device structure, the results and comparisons are discussed in Section IV, and the conclusions and future scope are discussed in Section V

## II. GATE ENGINEERED HEMT BIOSENSOR

In this section, the state of the art of some biosensors based on the gate-engineered AlGaN/GaN HEMTs was discussed. In recent years, few review articles have been published based on the AlGaN/GaN HEMT biosensors. GaN HEMT biosensors are primarily used in the field of biosensors due to their superior performance characteristics like non-toxicity, high sensitivity to variations on the surface charge, robust performance for different environmental conditions and high stability to chemical variations.[13], [14]. Due to these exceptional features of the AlGaN/GaN HEMTs in the field of biosensing, in this piece of research, we propose a gate-engineered AlGaN/GaN HEMT biosensor for detecting various cancers and viruses. One of the research projects reported in the literature on biosensors for pH detection focuses on the fabrication and characterization of a pH sensor developed for high sensitivity. The gate area used is oxide-based to confirm the device's performance for pH detection before metal probing and packaging. The dimensions of the gate ($L_G$ length, $W_G$ width), spacing between the gate and source ($L_{SG}$) and the spacing between gate and drain ($L_{GD}$) have been altered to investigate the effect on the sensitivity of the pH values[15]. A circular metal oxide semiconductor high-electron-mobility transistor (C-MOSHEMT) biosensor for pH detection has been developed. The key advantage of C-MOSHEMT over L-MOSHEMT is that the reduction in process cost, combined with a less complex design and increased coverage over the sensing area, is significantly enhanced [16]. The recessed gate AlGaN/GaN HEMT was developed to detect urea, and the same was fabricated and tested for various parameters, such as sensing sensitivity and transconductance, which were improved compared to the planar gate AlGaN/GaN ISFET urea biosensors; the methodology used is the photoelectrochemical method [17]. An analytical model is developed for MOSHEMT to detect biomolecules, including streptavidin, proteins, uricase, and ChOx. The sensitivity of the biomolecules is improved by altering the dielectric constant and length of the cavity with the dielectric modulation technique[18][19]. A similar sensor proposed for detecting cytochrome c, glucose, biotin, and uricase uses an approach based on a physics-based analytical model developed for an open-gate AlGaN/GaN HEMT. The device developed was easy to fabricate and operates at very low voltages, with improved sensitivity [19]. Ruby Mann *et al.* developed a physics-based analytical model for the electrical detection of biomolecules, including Zein, Biotin, ChOx, and Keratin. In this article, the authors assumed that the AlGaN layer is fully ionized and only one subband is occupied. The 2D density states and Fermi-Dirac statistics are used to generate self-consistent analytics of the carrier density and the quantum well at the AlGaN/GaN interface. The structure of the HMET comprises a dual gate, which improves resistance to short-channel effects over single-gate HEMT devices[20]. An AlGaN/GaN HEMT sensor designed and demonstrated is used to create a swift and simplistic immunoassay using aptamer functionalization. This sensor facilitates the detection of protein in a physiological salt environment. This overcomes the charge screening effects, without requiring sample preprocessing. The authors reported that the tunable and amplified sensitivity of the solution-gated electric double layer (EDL) AlGaN/GaN HMET biosensor's sensitivity is improved[21]. Recently, an AlGaN/GaN HEMT biosensor developed by Hui Chang et al. was used to detect hormone (Cortisol) that helps to manage blood pressure, glucose and stress. The gate geometry is optimized by adjusting the separation between the gate and the source and drain regions. The specificity, sensitivity and linearity have been analyzed for different gate structures [22]. Numerous gate-engineered GaN HEMTs have been developed for a long time, and there is no end to this; still, some researchers are working on these devices to enhance the performance metrics of the sensors.

## III. DEVICE STRUCTURE AND METHODOLOGY

In this section, we provide a detailed description of the device, specifically the proposed AlGaN/GaN HEMT shown in Figure 1(a), which exhibits a high 2DEG near the interface due to the addition of the AlN cap layer, thereby enhancing polarization and passivation. The device is grown on a sapphire substrate, which is a cost-effective material that helps reduce the overall cost of the device. The AlN cap layer introduces less polarization charge and a high 2DEG density, even though it exhibits higher electron mobility, improved DC electrical characteristics, and higher drain current, transconductance, and an improved ON/OFF ratio, with lower OFF resistance. SiN, GaN and AlN are the widely used cap layers; the device performance relies on the type of cap layer used. The most commonly used cap layer is AlN, which has a large bandgap (6.2 eV) and a reduced lattice mismatch with GaN.

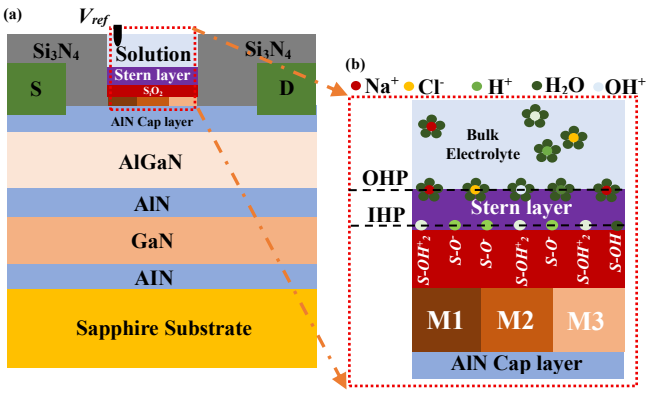



**Fig. 1** (a) The structure of gate-engineered AlGaN/GaN HEMT (b) Enlarged Sensing area for pH detection.

The device is grown on a Sapphire substrate, with a structure composed of different layers: an 18nm $Al_{0.2}Ga_{0.8}N$ barrier layer, a 2 nm AlN cap layer, a 1 nm AlN interlayer, a 1.5 nm undoped GaN layer, and a 100 nm AlN nucleation layer. To form a source and drain layer, materials such as Ti/Al/Ni/Au are used in sequence. The structure shown in Fig. 1(a) is the gate-engineered AlGaN/GaN HEMT. The advantage of gate engineering results in changes to various performance metrics, like drain current ($I_d$), transconductance ($g_m$), cutoff frequency, and RF current gain. These metrics are analyzed for triple material gate (TMG), dual material gate (DMG), and compared to a single material gate (SMG).

The sensitive region is enlarged and is illustrated in Fig. 1(b), which comprises different gate materials of identical lengths $L_1$, $L_2$ and $L_3$ = 40nm in this work, and all of these lengths are identical. The work function of these materials is chosen as $\emptyset_{M1}$ = 5.0 eV, $\emptyset_{M2}$ = 4.75 eV, $\emptyset_{M3}$ = 4.5 eV, whereas in the case of DMG, L1 and L2 will have identical lengths and are equal to 60 nm (this work) with similar work functions as stated earlier ($\emptyset_{M1}$ = 5.0 eV, $\emptyset_{M2}$ = 4.75 eV). The concept of gate engineering with different gate materials, in turn, enhances the efficiency of carrier transportation. The gate materials are arranged in such a way that the material having the lowest work function is placed near the drain and the highest towards the source terminals of the device. A distance of $L_{SG}$ and $L_{GD}$ separates the gate and source, as well as the drain and source. The typical dimensions

of these parameters are considered to be $L_{SG}$ = 1.5 µm and $L_{GD}$ = 2.96 µm in this work. The gate length of the simulated devices is 160 nm. The gate extends through the $S_iO_2$ layer up to the AlN cap layer, ensuring that the device operates in enhancement mode. The model parameters have been adjusted to closely align the simulated results with the experimental outcomes. The results demonstrate a strong agreement between the two, thereby validating our proposed device. The sensing area displays different planes, such as the outer Helmholtz plane (OHP), and another plane is formed due to the absorption of ionic charges on the insulator. It is known as the inner Helmholtz plane (IHP), which shows the maximum solvated ions at OHP as indicated in Fig.1(b). Both the IHP and OHP eventually form an electric double layer[23]. During the simulation, various models are incorporated into the SILVACO ATLAS code, including Concentration-dependent mobility (CONMOB), a mobility model that specifies the doping concentration of electrons and holes. CONMOB.N is used for the electrons, and CONMOB.H is used for the holes. Shockley-Read-Hall (SRH) is a recombination model that utilizes fixed minority carrier lifetimes. At the same time, Field-dependent mobility (FLDMOB) is another mobility model that specifies the lateral electric field dependency of electrons and holes. Methods and models are validated and incorporated into the simulation process. The pH sensor is modelled as a pH-dependent voltage source and an AlGaN/GaN HEMT, where the difference in effective gate voltage, Vg, eff, and the reference voltage, Vref, across the electrolyte is considered. The variation of the charges at the interface and the channel of conventional nano FETs and MOSFETs results from the changes in potential near the oxide/fluid interface, which is derived by[24]:

$$\Delta\sigma = -C_{ox}\Delta\psi_o = -\frac{\epsilon_o\epsilon_r}{t_{ox}}\Delta\psi_o \quad (1)$$

Where $\epsilon_r$ is the dielectric constant of the $S_iO_2$(3.9), $\Delta\psi_0$ is the surface potential charge at the interface (oxide/fluid), $C_{ox}$ is the capacitance of the oxide layer, and the oxide thickness is denoted by $t_{ox}$. When the gate oxide or the membrane (Sensing) is exposed to the electrolyte, this reaction tends to form an interface charge layer. The magnitude of the charge relies on the electrolyte's (pH's) ionic concentration, which in turn modulates the charge density of the interface (semiconductor-oxide). Hence, the change in the electrolyte (pH) is modelled as charge variation at the interface (AlGaN/oxide), and then there is a change in the charge in the 2DEG channel[25]. The electrolyte and interface charges can be modelled as a pH-dependent voltage source, where the effective surface potential can be described as follows[26], [24]:

$$\psi_o = -\log_e 10\times\delta_w\times\frac{K_BT}{q}\times\left(pH-pH_{pzc}\right) \quad (2)$$

$$\delta_w = \frac{\beta}{1+\beta} \quad (3)$$

$$\beta = q^2N_s\frac{\eta}{C_{eq}\times K_BT} \quad (4)$$

Where q is the electron charge, T is the temperature in Kelvin, $K_B$ is the Boltzmann constant, $\delta_w$ is expressed as in equation (3), and β is the sensitivity parameter expressed as in equation (4). The point of zero charge (pzc) of pH value is denoted as $pH_{pzc}$ (ref. equation (2)), and is given by $pH_{pzc} = {(pK_a+pK_b)}/{2}$, $pK_a$ = $-\log_{10}(K_a)$ and $pK_b$ = $-\log_{10}(K_b)$. Where $K_b$ and $K_a$ are the base and acid dissociation constants, respectively, are expressed as shown in equations (5) & (6).

$$K_b = \frac{[S\text{-}O^-]+[H_s^+]}{[S\text{-}OH]} \quad (5)$$

$$K_a = \frac{[S\text{-}OH]+[H_s^+]}{[S\text{-}OH_2^+]} \quad (6)$$

The values used for $pH_{pzc}$, $pK_a$ and $pK_b$ are 2, 6 and -2, respectively.[27].

The number of surface sites available relies on the type of material in contact with the electrolyte, as shown in the following equation.[28]

$$N_s = [SOH_2^+]+[SOH]+SO^- \quad (7)$$

With a fixed bond length, the number of available surface sites is physically limited. The number of surface sites for $S_iO_2$ is $5\text{x}10^{12}/\text{cm}^2$ and η in equation (4) is $2\times10^{-\left(\frac{\Delta pK}{2}\right)}$ and $\Delta pK = pK_b - pK_a$, the equivalent capacitance ($C_{eq}$) expressed as in equation (8).

$$C_{eq} = \frac{C_{DL}\times C_{stern}}{C_{DL}+C_{stern}} \quad (8)$$

$C_{DL}$ in equation (8) is the capacitance of the double layer and is expressed as shown in equations (9), and $C_{Stern}$ is the Stern layer capacitance, which is equal to $20\mu F/cm^2$[29].

$$C_{DL} = \sqrt{\frac{2Z_i^2q^2n_i\epsilon_w}{K_BT}} \quad (9)$$

The term $n_i$ refers to the ionic concentration, which is connected to the carrier concentration of an intrinsic semiconductor. It is calculated using the formula shown in (10)

$$n_i = N_CN_V\times e^{-E_g/2K_BT} \quad (10)$$

This value is obtained by multiplying the effective ionic concentration ($i_{eff}$) by Avogadro's number ($N_{avg}$ = $6.022\text{x}10^{23}$/mol). The result is then adjusted for use in /cm³ according to the relevant equation in (11).

$$n_i = i_{eff}\times N_{avg}\times\frac{1}{1000} \quad (11)$$

$$[S\text{-}OH_2^+] \rightleftharpoons [S\text{-}OH]+[H_s^+] \quad (12)$$

$$[S\text{-}OH] \rightleftharpoons [S\text{-}O^-]+[H_s^+] \quad (13)$$

In acidic conditions, the concentration of hydrogen ions $H_S^+$ is higher, which means that the left side of Equation (12) will be predominant. As a result, surface neutral species, known as SOH groups, will accept a proton to form an acceptor-type protonated species, $S\text{-}OH_S^+$. This process leads to a positively charged AlGaN surface, which tends to increase the concentration of 2DEG carriers and, consequently, the current. Conversely, in basic conditions where the concentration of hydroxide ions $OH^-$ exceeds that of hydrogen ions $H_S^+$. The right side of Equation (13) becomes dominant. In this scenario, the SOH species will release a proton, forming a donor-type deprotonated species. $S\text{-}O^-$. This results in a negatively charged AlGaN surface, which tends to decrease the concentration of 2DEG carriers and, therefore, reduce the current. The site-binding model of oxides demonstrates the amphoteric nature of both the electrolyte and the oxide surface through specific surface reactions. In this model, an oxide-bonded molecular site is represented as S, while OH denotes a hydroxyl group. When ions adsorb onto the specific surface hydroxyl groups, they create both positively and negatively charged sites on the sensing membrane ($S_iO_2$). This process results in the formation of protonated, ($SOH_2^+$) & deprotonated ($SO^-$) species from the amphoteric SOH sites, as illustrated in equations (12) & (13). The concentration of the hydrogen ions at the interface (electrolyte/$S_iO_2$) is $[H_s^+]$ and is equal to $10^{-pH}\times e^{-(q\psi_o/kT)}$ [20] The surface charge density due to this is given as in equation (14).

$$\sigma_o = q([SOH_2^+]-[SO^-]) \quad (14)$$

On solving equation (14), the surface charge density[41] in terms of acid and base dissociations, the number of surface sites is derived as follows:

$$\sigma_o = qN_s \left( \frac{\frac{[H_s^+]}{K_a} \frac{K_b}{[H_s^+]}}{\frac{[H_s^+]}{K_a} + \frac{K_b}{[H_s^+]} + 1} \right) \quad (15)$$

The surface charge density determined for various interface charge densities ($\sigma_{int}$), and hence the variation of the charge at the interface (oxide/fluid), effective surface potentials were determined (ref. equations (1) & (2)). The above analysis is conducted at different pH levels using 0.001 PBS (phosphate-buffered saline). As the point of zero charge ($pH_{pzc}$) is equal to 2, some of the calculated values have a negative sign, as shown in Table 1.

**Table 1.** Interface charge density($\sigma_{int}$) for various values of pH[25].

| pH Value | Interface charge density $\sigma_{int}$/cm$^2$ (0.001 X phosphate-buffered saline (PBS)) |
|---|---|
| 1 | $3.22x10^{11}$ |
| 2 | 0 |
| 3 | $-3.22x10^{11}$ |
| 4 | $-6.44x10^{11}$ |
| 5 | $-9.66x10^{11}$ |
| 6 | $-1.28x10^{12}$ |
| 7 | $-1.6x10^{12}$ |
| 8 | $-1.93x10^{12}$ |
| 9 | $-2.54x10^{12}$ |
| 10 | $-2.58x10^{12}$ |

The intrinsic semiconductor material shares similar properties with electrolyte solutions, as both are electrically charge-neutral. In an electrolyte solution, there are positive and negative ions, which are analogous to holes and electrons in a semiconductor. Both systems can be described by the Poisson equation and the Boltzmann distribution, allowing for accurate calculations of the mobile electrostatic charge distribution using the semiconductor model. This similarity helps to define equations for positive and negative ionic charges in relation to holes and electrons in the intrinsic semiconductor. [24], [27], [32], [33]. Various parameters of an intrinsic semiconductor were modified to simulate the behaviour of an electrolyte. This was accomplished by adjusting the dielectric constant of the semiconductor material to match that of water ($\epsilon_w = 78\ \epsilon_o$) and setting the mobilities of holes and electrons to correspond with those of $Na^+$ ($4.98 \times 10^{-4}$ cm²/Vs) and $Cl^-$ ($6.88 \times 10^{-4}$ cm²/Vs)[27]. The ions with valence 1 in an electrolyte are assumed to be 1:1, and the expression of PB (Poisson-Boltzmann) is written as in equation (16).

$$\frac{\partial^2\psi}{\partial x^2} = -\frac{q}{\epsilon_w}\left[C_o^{Na^+} e^{\left(-\frac{q\psi}{kT}\right)} - C_o^{Cl^-} e^{\left(\frac{q\psi}{kT}\right)}\right] \quad (16)$$

The PB expression in equation (16) is almost the same as that of the semiconductor equation, which excludes the Fermi-Dirac distribution of electrons and holes. The $C_o^{Cl^-}$ & $C_o^{Na^+}$ in equation (16) denotes the equilibrium ionic charge concentrations of $Cl^-$ & $Na^+$ respectively. The intrinsic semiconductor material is rewritten as in equation (17).

$$\frac{\partial^2\psi}{\partial x^2} = -\frac{q}{\epsilon_{si}}\left[p_o \frac{1+e^{\left(\frac{E_i-E_v}{kT}\right)}}{1+e^{\left(\frac{E_i-E_v}{kT}\right)} e^{\left(\frac{q\psi}{kT}\right)}} - n_o \frac{1+e^{\left(\frac{E_c-E_i}{kT}\right)}}{1+e^{\left(\frac{E_c-E_i}{kT}\right)} e^{\left(-\frac{q\psi}{kT}\right)}}\right] \quad (17)$$

Where $E_c$, $E_v$, $E_i$, $n_o$, and $p_o$ represent the conduction band, valence band, intrinsic Fermi energy levels, electron and hole concentrations, respectively.

## IV. RESULTS AND COMPARATIVE ANALYSIS

The device shown in Fig.1(a) is simulated using SILVACO TCAD using ATLAS without any biomolecules and single material gate to measure various characteristics as a fundamental requirement of the device, simulations are performed to extract I-V characteristics to understand device functionality, the output characteristics of the HEMT with AlN cap layer are shown in Figure 2(a), it is found that he max saturated drain current is around 175 mA, Figure 2(b) shows the transfer characteristics of the AlGaN/GaN HEMT with AlN cap layer and is observed that there is a shift in the threshold voltage.

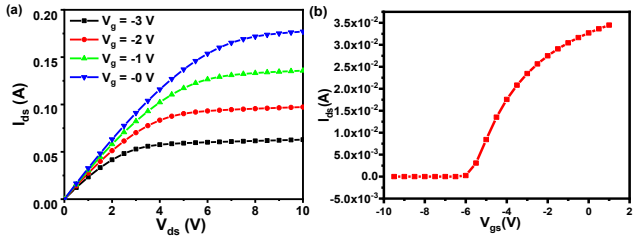



**Fig. 2** (a) Output characteristics of AlGaN/GaN HEMT with AlN cap layer (b) Transfer characteristics of AlGaN/GaN HEMT with AlN cap layer

The C-V characteristics curves of HEMT are measured. Based on these characteristic curves, the 2DEG beneath the gate is determined using the following expression, shown in equation (18)[34], [35], [36].

$$n_{2D} = \int_{V_T}^{V_G} \frac{CdV}{Sq} \quad (18)$$

Where C is the gate capacitance measured, S is the area of the gate Schottky contact, q is the charge of an electron, and $V_T$ is the threshold voltage, the C-V characteristics of the HEMT with an AlN cap layer are shown in Figure 3(a). The 2DEG density of the HEMT with an AlN cap layer has been improved. The variation of $n_{2d}$ with respect to various gate voltage values is plotted, as shown in Figure 3(b).

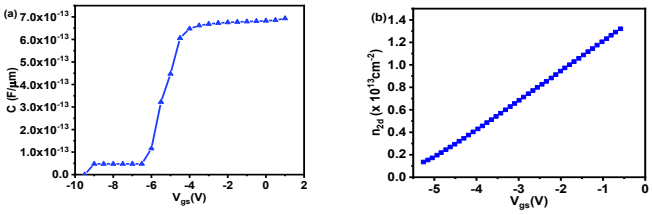



**Fig. 3** (a) C–V curves for AlGaN/GaN HEMT AlN cap layer. (b) 2DEG ($n_{2D}$) for various $V_{GS}$ in AlGaN/GaN HEMT with AlN cap layer.

With the addition of the AlN cap layer, the separation between the 2DEG channels and the Schottky metal increases, as shown by the maximum transconductance in Fig. 4(a). Furthermore, the effect of the AlN cap layer on the electron mobility beneath the gate area is extracted, and the resultant plot is depicted in Fig. 4(b). This plot is analyzed based on the carrier transport model using various scattering mechanisms.

The variation of channel potential along the lateral distance just below the sensing area is illustrated in Fig. 5(a). A cutline is drawn below the channel interface. As the pH of the electrolyte increases from 2 to 9, the channel potential decreases and remains unchanged due to the effect of the pH solution.

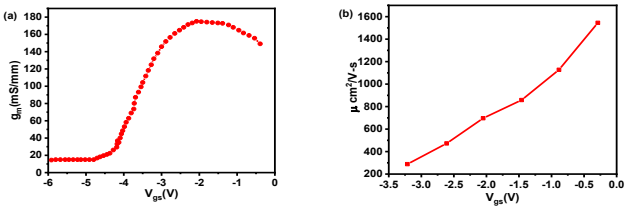



**Fig. 4** (a) Transconductance of AlGaN/GaN HEMT with AlN cap layer. (b) Electron mobility beneath the gate region of AlGaN/GaN HEMT with AlN cap layer.

However, there is a variation in the channel potential profile at the edges of the sensing region of the inner and outer fields. Fig. 5(b) shows the variation in total gate capacitance with changes in pH. The capacitance trend remains relatively flat until the threshold voltage, as no 2DEG charge is present. When the gate bias increases, a step-like response occurs around the threshold voltage due to the accumulation that takes place, because $C_{gg}$ predominantly depends on 2DEG concentration until the bias rises sufficiently to cause spillover. [37]. Figure 5(c) illustrates the relationship between drain bias and channel conductance at various pH levels. The intrinsic device has a channel conductance of 129 mS/mm, which decreases to 117 mS/mm when the pH is 9 and at zero bias (Vref = 0V).

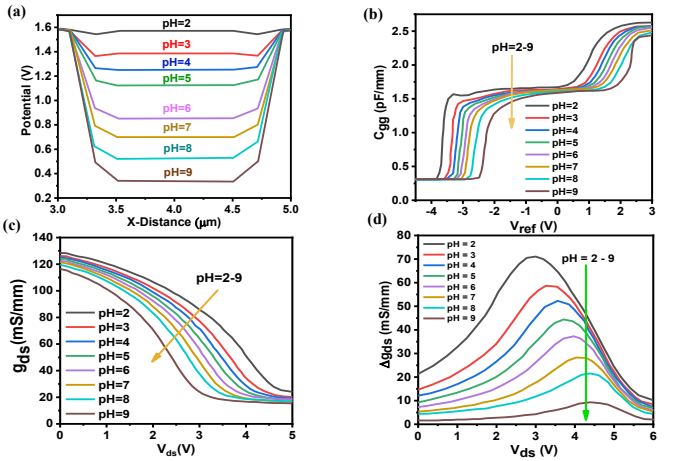
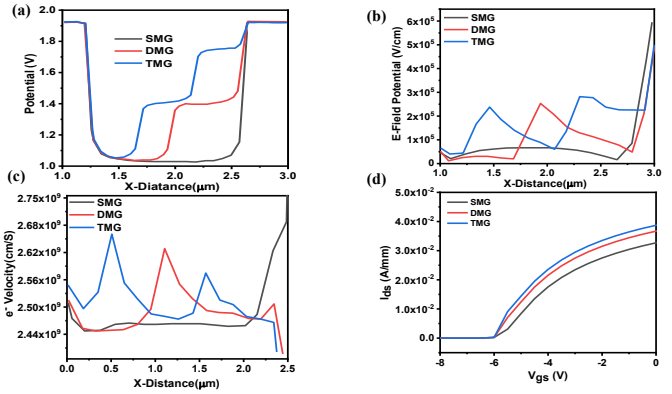



**Fig. 5** (a) Lateral channel potential underneath the sensing area (b) Variation of gate capacitance $C_{gg}$ for pH (2-9). (c) $V_{ds}$ vs Channel conductance $g_{ds}$ for pH (2-9). (d) $V_{ds}$ vs relative change in $\triangle g_{ds}$

Initially, the conductance is high because the channel contains the maximum number of carriers. However, as the pH increases, the channel conductance declines due to the capacitive coupling of additional interface charges at higher pH levels. The conductance curve shows a rapid decrease in conductance, indicating effective carrier confinement. Figure 5(d) presents the relative change in conductance for different pH levels, indicating that the variation in conductance increases until it reaches a peak around 3V, after which it diminishes in the saturation region. Therefore, it can be concluded that the device exhibits resistive behaviour in response to the applied drain bias and functions effectively as a resistive sensor. The variation of surface potential, lateral electric field and electron mobility along the channel for SMG, DMG and TMG is shown in Fig. 6 (a), (b) and (c), respectively. Fig. 6(d) shows the variation of the drain current for SMG, DMG and TMG. A smooth and nearly symmetrical potential profile is observed along the channel of the SMG device structure. In contrast, TMG and DMG devices exhibit an asymmetrical variation in potential along the channel. It has been verified that DMG structures feature a single step change in the potential profile at the interface between gate metals M1 and M2 (ref. Fig. 6 (a)). For the TMG structure, however, there are two-step changes in potential at the interfaces of gate metals M1 and M2, as well as M2 and M3 along the channel. This type of variation in surface potential likely enhances the screening of the channel region beneath the gate material M1 for the DMG structure, as well as for both M1 and M2 in the TMG structure. Simulated results indicate that, in the case of the TMG device, the variation in the slope of the surface potential at the drain side is less pronounced than that of the DMG and SMG devices. This results in a diminished electric field near the drain side. As a result, these devices have the potential to suppress short-channel effects (SCE), such as drain-induced barrier lowering (DIBL) and drain conductance, which increase with higher drain voltages. Additionally, the TMG device structure is less affected by hot carrier effects (HCEs) compared to the DMG and SMG structures. Furthermore, the potential profile clearly shows that the minimum channel potential occurs under the metal gate M1. This indicates that the threshold voltage and the characteristics of the TMG HEMT structure near the threshold will primarily be influenced by the controlling gate, which has the highest work function near the source end. The rise in the number of peaks in electric field variations improves carrier transport efficiency by facilitating carrier acceleration along the metal interface. In a traditional SMG device, there is only one peak in the electric field variation, which occurs at the drain side. Innovative DMG and TMG structures exhibit multiple peaks in their characteristics (ref. Fig. 6(b)). Specifically, the DMG device shows one peak near the drain side and another at the




interface between the gate metals M1 and M2.

**Fig. 6** (a) Surface potential along the channel, (b) Lateral electric field along the channel, (c) Electron mobility along the channel, (d) Drain characteristics for SMG, DMG and TMG.

Similarly, the TMG HEMT structures display three peaks: one at the drain side and the others at the interfaces between gate metals M2 and M3, and M2 and M1. The increase in the number of peaks for both DMG and TMG devices is mainly due to the surface potential steps along the channel. As a result, the discontinuity in the surface potential profile reduces the peak electric field at the drain side for these gate-engineered devices when compared to the SMG device. Notably, TMG structures yield impressive results by demonstrating fewer peaks in the electric field than both DMG and conventional HEMT devices. The reduced lateral electric field at the drain side of TMG and DMG devices enhances their average lifespan by minimizing hot carrier effects (HCEs). The peak lateral electric field near the source region enhances carrier acceleration at the metal interfaces, thereby improving carrier transport efficiency (CTE). As a result, the enhanced CTE in the novel TMG and DMG HEMT devices leads to faster speeds and increased drain current ($I_{ds}$) compared to conventional SMG devices. The comparison of electron velocity distribution profiles along the channel for TMG, DMG, and SMG structures at a drain-source voltage ($V_{DS}$) of 1 V is presented in Fig. 6(c). We observed that the

conventional SMG device exhibits monotonous behavior in its electron velocity distribution profiles. In contrast, our proposed structures display a varying number of peaks in the distribution, with the number of peaks increasing from DMG to TMG devices. This variation is primarily attributed to the presence of lateral electric field peaks in the electric field distribution profiles of these novel device structures. The transfer characteristics of gate-engineered TMG, DMG, and conventional SMG devices at a drain bias of 1 V are shown in Fig. 6(d). The results indicate that the proposed TMG and DMG structured devices achieve higher drain current densities of 39 mA/mm and 37 mA/mm, respectively, compared to the SMG device, which has a drain current density of 32.5 mA/mm. These improvements in current densities for gate-engineered HEMT devices are due to an increase in electron velocity and the lateral electric field near the source region. Enhanced carrier transport efficiency accelerates the carriers more effectively along the device channel.

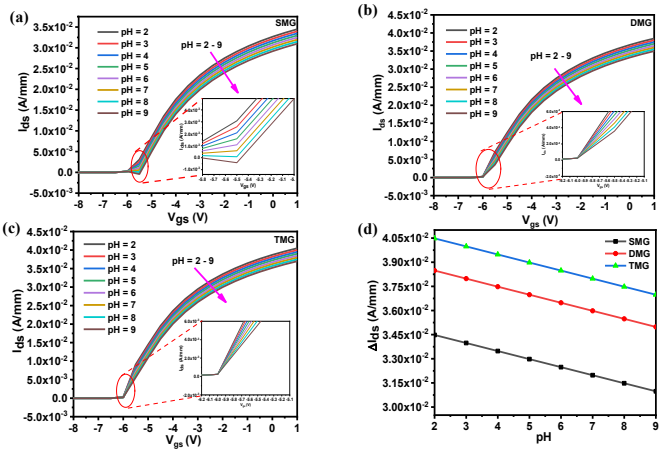



**Fig. 7** Transfer characteristics for pH = 2-9, (a) SMG, (b) DMG, (c) TMG, (d) Change in drain current with respect to pH from 2 to 9 of SMG, DMG and TMG.

The drain characteristics of AlGaN/GaN HEMTs are presented in Fig. 7, featuring three different gate structures. Fig. 7 (a), (b) and (c) show the drain characteristics of SMG, DMG and TMG, respectively. The pH values range from 2 to 9, there is an improvement in the resulting drain current of TMG compared to SMG and DMG (ref. Table. 1). It is observed that there is some steepness in the drain current, as indicated by a rise in pH value at $V_{gs}$ = -5.5V, the same is shown in the magnified area in Fig. 7 (a), and this steepness has been reduced for DMG and TMG as shown magnified area of Fig. 7 (b) and (c) respectively. Fig. 7(d) illustrates the variation in drain current with respect to pH, spanning a range from 2 to 9. It is observed that the TMG has a high drain current ($I_{ds}$ = 40.48 mA at pH = 2). The variation of the lateral electric field potential for pH from 2 to 9 with respect to the position from source to drain along the channel is shown in Fig. 8 (a), (b) and (c) for SMG, DMG and TMG, respectively. This electric field potential has its minimum value towards the source end and its maximum value at the drain end. It is also observed that there is a single peak in SMG and multiple peaks in the DMG and TMG. For the DMG device, one peak is detected near the drain side, and another peak is observed at the interface between gate metals M1 and M2. In contrast, the novel TMG HEMT structures exhibit three peaks: one peak at the drain side and the other two at the interfaces between gate metal M2 and M3, as well as between M2 and M1. Fig. 8(d) is a plot of the lateral electric field potential versus pH, ranging from 2 to 9. It is observed that there is a variation in the potential along the channel for SMG, DMG and TMG. he comparison of the lateral electric field potential at a distance of 2.9 µm (approximately) of SMG, DMG and TMG for pH = 2 and 9 is shown in the Table. 2. Further, we extend our analysis of the pH sensor for surface potential along the channel.

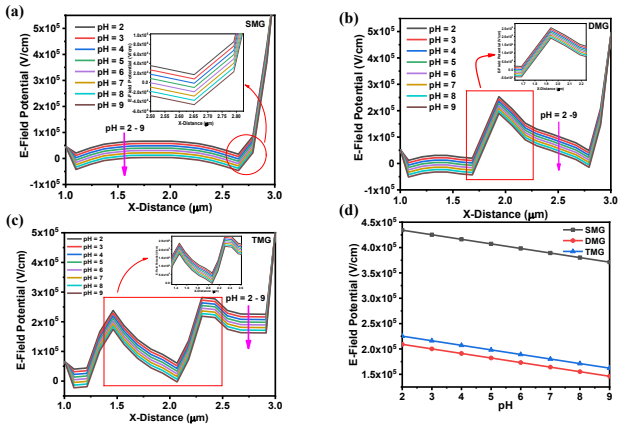



**Fig. 8** Lateral electric field potential for pH = 2-9, (a) SMG, (b) DMG, (c) TMG, (d) Change in electric field with respect to pH from 2 to 9 of SMG, DMG and TMG.

The variation of the surface potential along the channel of SMG, DMG and TMG structures for pH = 2-9 is shown in Fig. 9 (a), (b) and (c), respectively. The potential profile of the SMG is symmetrical, while the other two (DMG and TMG) have an asymmetrical profile. The DMG structure shows a single step change in the potential profile at the interface between the gate metals M1 and M2. In contrast, the TMG structure exhibits two-step changes at the interfaces of gate metals M1 and M2, as well as M2 and M3, along the channel. This variation in surface potential likely enhances the screening effect in the channel region beneath gate metal M1 for the DMG structure and beneath metals M1 and M2 for the TMG structure. Simulation results indicate that the slope of the surface potential at the drain side is less pronounced in the TMG device compared to the DMG and SMG devices. The change in surface potential with respect to pH, ranging from 2 – 9 for SMG, DMG and TMG structures, is shown in Fig. 9(d). The comparison of the surface potential at a distance of 2.4 µm (approximately) of SMG, DMG and TMG for pH = 2 and 9 is shown in the Table. 2.

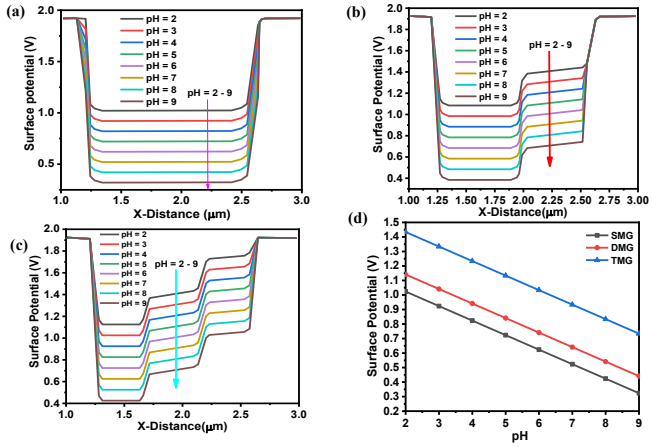



**Fig. 9** Surface potential for pH = 2-9, (a) SMG, (b) DMG, (c) TMG, (d) Change in surface potential with respect to pH from 2 to 9 of SMG, DMG and TMG.

A few performance metrics of the Gate-engineered AlGaN/GaN HEMT with different gate structures.

**Table. 2: Comparison between SMG, DMG and TMG with respect to pH values**

| Gate Structure → | SMG | | DMG | | TMG | |
|---|---|---|---|---|---|---|
| pH value → | 2 | 9 | 2 | 9 | 2 | 9 |
| Drain current (mA/mm) | 34.48 | 30.98 | 38.48 | 34.98 | 40.48 | 36.98 |
| Lateral Electric Field Potential (V/Cm) | $4.34\times10^5$ | $2.92\times10^5$ | $2.09\times10^5$ | $1.46\times10^5$ | $2.25\times10^5$ | $1.53\times10^5$ |
| Surface Potential (V) | 1.02 | 0.32 | 1.44 | 0.74 | 1.75 | 1.05 |

The performance of TMG structures is superior to that of the other two structures. The sensitivity of the proposed HEMT for three different gate structures (SMG, DMG, and TMG) is determined from its drain characteristics by considering the variation of drain current with respect to the pH value, as depicted in Figs. 10(a), (c), and (e). It is observed that the drain current decreases with an increase in pH value, ranging from 2 to 9. From these responses, it is clear that the device shows good sensitivity for all three structures. The following expression 19 calculates the sensitivity for pH = 2. [38],[39].

$$S_I = \left(\frac{\Delta I_{ds}}{\Delta pH}\right) = \left(\frac{I_{ds_{pH2}} - I_{ds_{pH(2-9)}}}{abs(pH_2 - pH_{(2-9)})}\right) \quad (19)$$

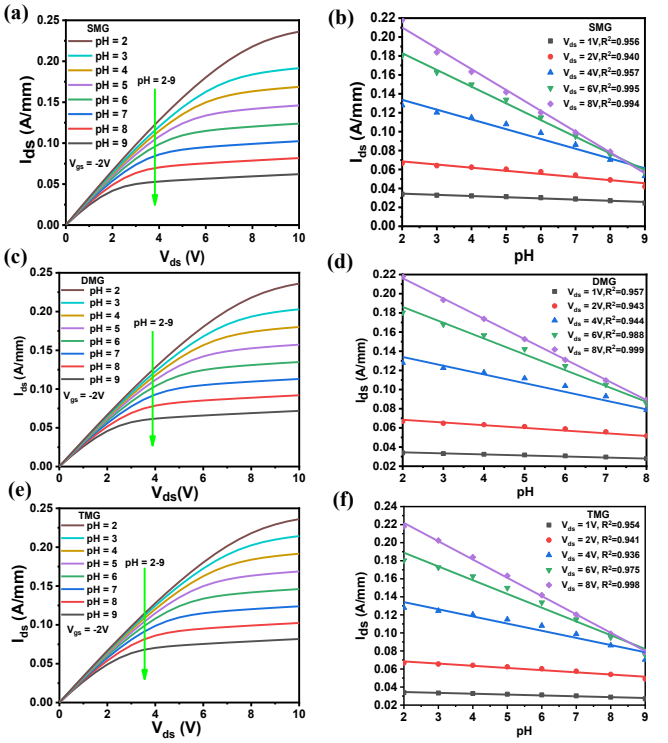



**Fig. 10** Drain current ($I_{ds}$) in response to the variation in drain voltage $V_{ds}$ = 0-10 V at $V_{gs}$ =-2V, and Comparison of sensitivities at different $V_{ds}$ (a, b) SMG, (c, d) DMG and (e, f) TMG.

The current sensitivities were calculated for different values of $V_{ds}$ = 1, 2, 4, 6, and 8V, while $V_{gs}$ = -2V. The sensitivity values for SMG, DMG and TMG are shown in Table 3. The linear relationship is measured for various values of $I_{ds}$ and pH at $V_{ds}$ = 1, 2, 4, 6, and 8 V, with $V_{gs}$ = -2V (Fig. 10(b), (d), and (e)). The coefficient of determination $R^2$ is also calculated to analyze the linear fit for all three gate structures. The reliable sensing performance is noticed as the drain current decreases with an increase in pH value. The values of R2, which are greater than 0.96, justify that the drain current decreases linearly with an increase in pH. This indicates that the proposed HEMT sensor exhibits high predictability. The voltage sensitivity is also determined for three structures, at different reference currents ($I_{ds}$-A/mm). At drain current $I_{ds}$ = 0.001 A/mm, three structures (SMG, DMG and TMG) cover the sensitivity of ≈49.1 mV/pH [SMG], with $R^2 \approx 1.0$, indicating perfect linearity. Similarly, at $I_{ds}$ = 0.005 A/mm, the sensitivity ≈is 44 mV/pH, with R2 ≈ 0.982, SMG shows the best balance between the high sensitivity and linearity as shown in the table. 3. These values are near the Nernst limit (~59 mV/pH) and are typical for well-designed ISFET and HEMT pH sensors operating within practical conditions. In this study, the proposed HEMT with different gate structures exhibits the maximum current sensitivities. For SMG, the sensitivity is 23.20 mA/mm/pH, for DMG, the sensitivity is 21.52 mA/mm/pH, and for TMG, the sensitivity is 19.81 mA/mm/pH. The work carried out for different performance parameters is depicted in the Table. 3, and the current sensitivities are compared with different gate structures.

**Table. 3: The sensitivity values for SMG, DMG and TMG**

| $V_{ds}$ (V) | Current Sensitivity (mA/mm/pH) for pH = 2-8 (@$V_{gs}$ = -2V) | | | | | | Ref. | Voltage Sensitivity (mV/pH) @0.01 A/mm | | |
|---|---|---|---|---|---|---|---|---|---|---|
| | THIS WORK | | | | | | | THIS WORK | | |
| | SMG | $R^2$ | DMG | $R^2$ | TMG | $R^2$ | | SMG | DMG | TMG |
| 1.00 | 1.14 | 0.956 | 0.98 | 0.957 | 0.85 | 0.954 | 0.14[33] | 44.2 | 36.4 | 49.1 |
| 2.00 | 2.95 | 0.940 | 2.50 | 0.943 | 2.12 | 0.941 | 1.4[41] | | | |
| 4.00 | 9.59 | 0.957 | 8.22 | 0.944 | 6.96 | 0.936 | 3.4[33] | | | |
| 6.00 | 17.48 | 0.995 | 15.85 | 0.988 | 14.20 | 0.975 | -- | | | |
| 8.00 | 23.20 | 0.994 | 21.52 | 0.999 | 19.81 | 0.998 | -- | | | |

## V. CONCLUSION

The gate-engineered AlGaN/GaN HEMT biosensor proposed in this article features a high-performance device with various gate structures. The gate structure of the HEMT is analysed for three different gate structures, each utilising three different gate materials (SMG, DMG, and TMG). The performance of the SMG is compared with that of the DMG and TMG; the response of these structures to pH provides good sensitivity and better performance. These gate engineering techniques help optimise performance parameters, such as microwave, RF, and mixed-signal applications. There is a good linear relationship $I_{ds}$ and pH. The determination of the coefficient $R^2$ is nearly equal to 0.96 for all three structures, given the current sensitivity of pH. We emphasise that performing practical gate engineering can significantly enhance the sensor's response. These findings establish the proposed gate-engineered AlGaN/GaN HEMT as a highly sensitive and reliable candidate for next-generation pH-sensing technologies.


## ACKNOWLEDGEMENT

The authors acknowledge ANRF (*Anusandhan National Research Foundation*), Govt. of India sponsored "*Visiting Advanced Joint Research Faculty Scheme*" (VAJRA) Project No. VJR/2021/000024, and "*Mathematical Research Impact Centric Support*" (MATRICS) Project No. MTR/2021/000370 for support.


## DECLARATIONS

The authors declare that they have no conflict of interest.

## REFERENCES


[1] N. Olson and J. Bae, "Biosensors—Publication Trends and Knowledge Domain Visualization," *Sensors*, vol. 19, no. 11, p. 2615, Jun. 2019, doi: 10.3390/s19112615.

[2] M. Burra, A. K. Johar, V. Kanungo, and A. Kumar, "Optimizing AlGaN/GaN MOS-HEMT architecture for enhanced sensing of neutral and charged biomolecules," *J. Alloys Compd.*, vol. 1015, p. 178814, Feb. 2025, doi: 10.1016/j.jallcom.2025.178814.

[3] Y. Liu *et al.*, "Enhancement of Sensing Performance of GaN-Based MOS-HEMT Biosensors by Graded AlGaN Barrier," *IEEE Sens. J.*, vol. 24, no. 15, pp. 23470–23479, Aug. 2024, doi: 10.1109/JSEN.2024.3409708.

[4] R. Poonia, C. Periasamy, A. M. Bhat, L. Bhargava, and C. Sahu, "Performance Assessment of AlGaN/GaN HEMT for Human Serum Albumin Detection Using Charge Deduction Methodology," *IEEE Sens. J.*, vol. 24, no. 10, pp. 15784–15792, May 2024, doi: 10.1109/JSEN.2024.3385496.

[5] H. M. Pardeshi, G. Raj, S. Pati, N. Mohankumar, and C. K. Sarkar, "Performance assessment of gate material engineered AlInN/GaN underlap DG MOSFET for enhanced carrier transport efficiency," *Superlattices Microstruct.*, vol. 60, pp. 10–22, 2013, doi: 10.1016/j.spmi.2013.04.019.

[6] G. P. Rao, T. R. Lenka, and H. P. T. Nguyen, "Performance Analysis of Gate Engineered III-Nitride/ $\beta$-Ga 2 O 3 Nano-HEMT for High-Power Nanoelectronics," in *2023 IEEE International Symposium on Circuits and Systems (ISCAS)*, May 2023, pp. 1–4, doi: 10.1109/ISCAS46773.2023.10181917.

[7] M. T. Bin Kashem and S. Subrina, "Analytical modeling of channel potential and threshold voltage of triple material gate AlGaN/GaN HEMT including trapped and polarization-induced charges," *Int. J. Numer. Model. Electron. Networks, Devices Fields*, vol. 32, no. 1, Jan.

2019, doi: 10.1002/jnm.2476.

[8] S. Adak, S. K. Swain, H. Rahaman, and C. K. Sarkar, “Impact of gate engineering in enhancement mode n++GaN/InAlN/AlN/GaN HEMTs,” *Superlattices Microstruct.*, vol. 100, pp. 306–314, Dec. 2016, doi: 10.1016/j.spmi.2016.09.025.

[9] G. Purnachandra Rao, T. Ranjan Lenka, and H. Pham Trung Nguyen, “Analysis of Channel length, Gate length and Gate position Optimization of III-Nitride/β-Ga2O3 Nano-HEMT for High-Power Nanoelectronics and Terahertz Applications,” *Mater. Sci. Eng. B*, vol. 293, p. 116498, Jul. 2023, doi: 10.1016/j.mseb.2023.116498.

[10] D. R. Androse, S. Deb, S. K. Radhakrishnan, and E. Sekar, “T-gate ALGaN/GaN HEMT with effective recess engineering for enhancement mode operation,” in *Materials Today: Proceedings*, 2021, vol. 45, pp. 3556–3559, doi: 10.1016/j.matpr.2020.12.1076.

[11] T. R. Lenka, G. N. Dash, and A. K. Panda, “2DEG transport in gate recessed AlGaN/(InGaN)/GaN HEMT,” in *2013 IEEE International Conference of Electron Devices and Solid-state Circuits*, Jun. 2013, pp. 1–2, doi: 10.1109/EDSSC.2013.6628042.

[12] G. P. Rao, T. R. Lenka, N. E. I. Boukort, and H. P. T. Nguyen, “Investigation of <scp>DC</scp> and <scp>RF</scp> characteristics of spacer layer thickness engineered recessed gate and field-plated III-nitride nano-HEMT on <scp> β-Ga $_2$ O $_3$ </scp> substrate,” *Int. J. Numer. Model. Electron. Networks, Devices Fields*, vol. 37, no. 1, Jan. 2024, doi: 10.1002/jnm.3138.

[13] C. Li, X. Chen, and Z. Wang, “Review of the AlGaN/GaN High-Electron-Mobility Transistor-Based Biosensors: Structure, Mechanisms, and Applications,” *Micromachines*, vol. 15, no. 3, p. 330, Feb. 2024, doi: 10.3390/mi15030330.

[14] L. Repaka, J. Ajayan, S. Bhattacharya, B. Mounika, A. Akshaykranth, and D. Nirmal, “A review of microelectronic AlGaN/GaN HEMT biosensors for the detection of various cancer diseases and bacterial/viral pathogens,” *Microsyst. Technol.*, Dec. 2024, doi: 10.1007/s00542-024-05835-4.

[15] A. Varghese, P. Chinnamuthan, and L. Bhargava, “Fabrication and pH-Sensitivity Analysis of MOS-HEMT Dimensional Variants for Bio-Sensing Applications,” *IEEE Trans. Nanobioscience*, vol. 20, no. 1, pp. 28–34, 2021, doi: 10.1109/TNB.2020.3023725.

[16] A. Varghese, C. Periasamy, L. Bhargava, S. Bin Dolmanan, and S. Tripathy, “Fabrication and Modeling-Based Performance Analysis of Circular GaN MOSHEMT-Based Electrochemical Sensors,” *IEEE Sens. J.*, vol. 21, no. 4, pp. 4216–4224, Feb. 2021, doi: 10.1109/JSEN.2020.3032175.

[17] C. T. Lee and Y. S. Chiu, “Gate-Recessed AlGaN/GaN ISFET Urea Biosensor Fabricated by Photoelectrochemical Method,” *IEEE Sens. J.*, vol. 16, no. 6, pp. 1518–1523, Mar. 2016, doi: 10.1109/JSEN.2015.2506986.

[18] P. Pal, Y. Pratap, M. Gupta, and S. Kabra, “Modeling and Simulation of AlGaN/GaN MOS-HEMT for Biosensor Applications,” *IEEE Sens. J.*, vol. 19, no. 2, pp. 587–593, Jan. 2019, doi: 10.1109/JSEN.2018.2878243.

[19] E. Raghuveera, T. R. Lenka, G. P. Rao, V. Vadalà, and H. P. T. Nguyen, “Development of a physics-based 2DEG analytical and simulation model of AlGaN/GaN HEMT biosensor for biomolecule detection—an algorithmic approach,” *Microsyst. Technol.*, vol. 6, 2024, doi: 10.1007/s00542-024-05825-6.

[20] P. Pal, Y. Pratap, M. Gupta, and S. Kabra, “Open gate AlGaN/GaN HEMT biosensor: Sensitivity analysis and optimization,” *Superlattices Microstruct.*, vol. 156, p. 106968, Aug. 2021, doi: 10.1016/j.spmi.2021.106968.

[21] R. Mann, S. Rewari, S. Sharma, and R. S. Gupta, “Dual gate AlGaN/GaN MOS-HEMT biosensor for electrical detection of biomolecules-analytical model,” *Semicond. Sci. Technol.*, vol. 38, no. 3, p. 035012, Mar. 2023, doi: 10.1088/1361-6641/acb0f3.

[22] T.-Y. Tai *et al.*, “Design and Demonstration of Tunable Amplified Sensitivity of AlGaN/GaN High Electron Mobility Transistor (HEMT)-Based Biosensors in Human Serum,” *Anal. Chem.*, vol. 91, no. 9, pp. 5953–5960, May 2019, doi: 10.1021/acs.analchem.9b00353.

[23] H. Chang, B. Xu, G. Yang, Z. Gu, and J. Li, “Optimization of gate structure towards high-sensitivity AlGaN/GaN HEMT cortisol detection,” *Electroanalysis*, vol. 37, no. 1, Jan. 2025, doi: 10.1002/elan.202400143.

[24] M. Waleed Shinwari, M. Jamal Deen, and D. Landheer, “Study of the electrolyte-insulator-semiconductor field-effect transistor (EISFET) with applications in biosensor design,” *Microelectron. Reliab.*, vol. 47, no. 12, pp. 2025–2057, Dec. 2007, doi: 10.1016/j.microrel.2006.10.003.

[25] P. Dwivedi, R. Singh, and Y. S. Chauhan, “Crossing the Nernst Limit (59 mV/pH) of Sensitivity Through Tunneling Transistor-Based Biosensor,” *IEEE Sens. J.*, vol. 21, no. 3, pp. 3233–3240, Feb. 2021, doi: 10.1109/JSEN.2020.3025975.

[26] Y. Dong *et al.*, “AlGaN/GaN heterostructure pH sensor with multi-sensing segments,” *Sensors Actuators, B Chem.*, vol. 260, pp. 134–139, 2018, doi: 10.1016/j.snb.2017.12.188.

[27] L. Wang, L. Li, T. Zhang, X. Liu, and J. P. Ao, “Enhanced pH sensitivity of AlGaN/GaN ion-sensitive field effect transistor with Al 2 O 3 synthesized by atomic layer deposition,” *Appl. Surf. Sci.*, vol. 427, pp. 1199–1202, Jan. 2018, doi: 10.1016/j.apsusc.2017.09.072.

[28] R. Narang, M. Saxena, and M. Gupta, “Analytical Model of pH sensing Characteristics of Junctionless Silicon on Insulator ISFET,” *IEEE Trans. Electron Devices*, vol. 64, no. 4, pp. 1742–1750, Apr. 2017, doi: 10.1109/TED.2017.2668520.

[29] R. E. G. van Hal, J. C. T. Eijkel, and P. Bergveld, “A novel description of ISFET sensitivity with the buffer capacity and double-layer capacitance as key parameters,” *Sensors Actuators B Chem.*, vol. 24, no. 1–3, pp. 201–205, Mar. 1995, doi: 10.1016/0925-4005(95)85043-0.

[30] P. Dak and M. A. Alam, “FET pH Sensor Model,” *nanoHUB*, pp. 1–16, 2014, [Online]. Available: https://nanohub.org/publications/11/1.

[31] A.-C. Salaün, F. Le Bihan, and T. Mohammed-Brahim, “Modeling the high pH sensitivity of Suspended Gate Field Effect Transistor (SGFET),” *Sensors Actuators B Chem.*, vol. 158, no. 1, pp. 138–143, Nov. 2011, doi: 10.1016/j.snb.2011.05.056.

[32] R. E. G. van Hal, J. C. T. Eijkel, and P. Bergveld, “A general model to describe the electrostatic potential at electrolyte oxide interfaces,” *Adv. Colloid Interface Sci.*, vol. 69, no. 1–3, pp. 31–62, Dec. 1996, doi: 10.1016/S0001-8686(96)00307-7.

[33] E. Patrick, M. Choudhury, and M. E. Law, “Simulation of the pH Sensing Capability of an Open-Gate GaN-Based Transistor,” *ECS Trans.*, vol. 69, no. 13, pp. 15–23, Sep. 2015, doi: 10.1149/06913.0015ecst.

[34] I.-Y. Chung, H. Jang, J. Lee, H. Moon, S. M. Seo, and D. H. Kim, “Simulation study on discrete charge effects of SiNW biosensors according to bound target position using a 3D TCAD simulator,” *Nanotechnology*, vol. 23, no. 6, p. 065202, Feb. 2012, doi: 10.1088/0957-4484/23/6/065202.

[35] M. Zhang *et al.*, “Influence of Fin Configuration on the Characteristics of AlGaN/GaN Fin-HEMTs,” *IEEE Trans. Electron Devices*, vol. 65, no. 5, pp. 1745–1752, May 2018, doi: 10.1109/TED.2018.2819178.

[36] P. Cui *et al.*, “InAlN/GaN HEMT on Si With fmax = 270 GHz,” *IEEE Trans. Electron Devices*, vol. 68, no. 3, pp. 994–999, Mar. 2021, doi: 10.1109/TED.2021.3049316.

[37] G. Jiang, Y. Lv, Z. Lin, Y. Liu, M. Wang, and H. Zhou, “The relationship between AlGaN barrier layer thickness and polarization Coulomb field scattering in AlGaN/GaN heterostructure field-effect transistors,” *Superlattices Microstruct.*, vol. 156, p. 106987, Aug. 2021, doi: 10.1016/j.spmi.2021.106987.

[38] H.-Y. Liu *et al.*, “Investigation of AlGaN/GaN Ion-Sensitive Heterostructure Field-Effect Transistors-Based pH Sensors With Al $_2$ O $_3$ Surface Passivation and Sensing Membrane,” *IEEE Sens. J.*, vol. 16, no. 10, pp. 3514–3522, May 2016, doi: 10.1109/JSEN.2016.2531107.

[39] L. Wang, L. Li, T. Zhang, X. Liu, and J.-P. Ao, “Enhanced pH sensitivity of AlGaN/GaN ion-sensitive field effect transistor with Al2O3 synthesized by atomic layer deposition,” *Appl. Surf. Sci.*, vol. 427, pp. 1199–1202, Jan. 2018, doi: 10.1016/j.apsusc.2017.09.072.

[40] D. Xue *et al.*, “Enhancing the sensitivity of the reference electrode free AlGaN/GaN HEMT based pH sensors by controlling the threshold voltage,” *Sensors Actuators B Chem.*, vol. 306, p. 127609, Mar. 2020, doi: 10.1016/j.snb.2019.127609.

[41] M. Sciullo, M. Choudhury, E. Patrick, and M. E. Law, “Optimization of GaN-Based HEMTs for Chemical Sensing: A Simulation Study,” *ECS Trans.*, vol. 75, no. 16, pp. 259–264, Aug. 2016, doi: 10.1149/07516.0259ecst.